Seismic observations of large-scale deformation at the bottom of fast-moving plates

Eric Debayle *, Yanick Ricard

Laboratoire de Géologie de Lyon: Terre, Planètes et Environnement, 2 rue Raphaël Dubois, Bâtiment Géode, 69622 Villeurbanne Cedex, France

ABSTRACT

We present a new tomographic model of azimuthal anisotropy in the upper mantle, DR2012, and discuss in details the geodynamical causes of this anisotropy. Our model improves upon DKP2005 seismic model (Debayle et al., 2005) through a larger dataset (expanded by a factor $\sim$ 3.7) and a new approach which allows us to better extract fundamental and higher-mode information. Our results confirm that on average, azimuthal anisotropy is only significant in the uppermost 200–250 km of the upper mantle where it decreases regularly with depth. We do not see a significant difference in the amplitude of anisotropy beneath fast oceanic plates, slow oceanic plates or continents. The anisotropy projected onto the direction of present plate motion shows a very specific relation with the plate velocity; it peaks in the asthenosphere around 150 km depth, it is very weak for plate velocities smaller than 3 cm yr^{-1}, increases significantly between 3 and 5 cm yr^{-1}, and saturates for plate velocities larger than 5 cm yr^{-1}. Plate-scale present-day deformation is remarkably well and uniformly recorded beneath the fastest-moving plates (India, Coco, Nazca, Australia, Philippine Sea and Pacific plates). Beneath slower plates, plate-motion parallel anisotropy is only observed locally, which suggests that the mantle flow below these plates is not controlled by the lithospheric motion (a minimum plate velocity of around 4 cm yr^{-1} is necessary for a plate to organize the flow in its underlying asthenosphere). The correlation of oceanic anisotropy with the actual plate motion in the shallow lithosphere is very weak. A better correlation is obtained with the fossil accretion velocity recorded by the gradient of local seafloor age. The transition between frozen-in and active anisotropy occurs across the typical $\sqrt{\text{age}}$ isotherm that defines the bottom of the thermal lithosphere around 1100 °C. Under fast continents (mostly under Australia and India), the present-day velocity orients also the anisotropy in a depth range around 150–200 km depth which is not deeper than what is observed under oceans.

© 2013 Elsevier B.V. All rights reserved.

1. Introduction

The first observations of seismic anisotropy date from the early sixties (Aki and Kanimura, 1963; McEvilly, 1964; Hess, 1964). Tomographic studies, at the end of the seventies and during the eighties, confirmed its presence at global scale in the oceanic and continental upper mantle (Forsyth, 1975; Lévêque and Cara, 1983; Tanimoto and Anderson, 1984; Regan and Anderson, 1984; Nataf et al., 1984; Montagner and Tanimoto, 1991). This anisotropy was attributed to the lattice preferred orientation of anisotropic crystals in minerals such as olivine or pyroxene (Nicolas and Christensen, 1987; Babuška and Cara, 1991).

Since the early nineties, the dramatic increase in the number of seismic stations and the development of automated approaches for analysis of very large datasets (Trampert and Woodhouse, 1995; van Heijst and Woodhouse, 1997; Debayle, 1999;

Beucler et al., 2003; Lebedev et al., 2005) sharpened the details of the anisotropic structure of the upper mantle (Park and Levin, 2002; Trampert and Woodhouse, 2003; Debayle et al., 2005; Beucler and Montagner, 2006; Panning and Romanowicz, 2006; Lebedev and van der Hilst, 2008; Ekstrom, 2011). Current global tomographic models now resolve anisotropic lateral variations with wavelengths greater than 1000 km, compared to 5000 km in the early eighties.

Despite this tremendous progress, the origin of seismic anisotropy is still debated. Shear-wave splitting (SKS) observations are commonly used to study upper mantle anisotropy, especially beneath continents. SKS-type phases provide lateral resolution of a few tens of kilometers beneath a seismic station. However, they integrate the anisotropy over the whole mantle and have no depth resolution. This lack of vertical resolution has fueled a long debate on the origin of anisotropy beneath continents. Where fossil geological trends are parallel to present-day plate motions, like under South Africa, the same SKS anisotropic directions can either be interpreted as related to present-day plate motions (Vinnik et al., 1995), or as frozen-in within the lithosphere (Silver et al., 2001).

At global scale, shear-wave splitting (SKS) observations have also either been interpreted as frozen-in lithospheric anisotropy from past deformation processes (Silver and Chan, 1988, 1991), or as asthenospheric anisotropy resulting from present-day shear induced by plate motions (Vinnik et al., 1992).

Surface waves provide global coverage of the upper mantle, and allow to study anisotropy in oceanic areas where few seismic stations are available. They are sensitive to both radial and azimuthal anisotropy. In the range of periods commonly used for upper mantle studies (40–300 s) they constrain the anisotropy with a limited lateral resolution of several hundreds of kilometers, but with a much better vertical resolution of few tens of kilometers. Surface wave and SKS observations are therefore complementary.

Global models of surface wave azimuthal anisotropy display strong correlations of fast axes with plate motions at asthenospheric depths (Debayle et al., 2005; Ekstrom, 2011). This is certainly true under fast oceans (Smith et al., 2004; Maggi et al., 2006) or continents like Australia (Lévêque et al., 1998; Debayle, 1999; Debayle and Kennett, 2000b; Simons et al., 2002) or India (Debayle et al., 2005). This supports the idea that at least part of the anisotropy originates in the asthenosphere and reflects present-day shear induced by plate motions. This interpretation is substantiated by the general agreement between anisotropy and the global mantle flow that can be computed from geodynamic model (Becker et al., 2007; Long and Becker, 2010).

Resolving surface wave anisotropic directions at small scale and with a vertical resolution sufficient to identify frozen-in deformation within the continental lithosphere remains a challenge. In the shallowest 150 km of the Australian lithosphere, the anisotropy seems frozen-in and preserved since the Alice Spring orogeny (Debayle and Kennett, 2000b; Simons et al., 2002). Under South Africa (Adam and Lebedev, 2012) and North America (Marone and Romanowicz, 2007; Yuan and Romanowicz, 2010), a likely frozen-in anisotropy aligned with the surface geological trends is underlaid by the asthenosphere where fast anisotropic directions are coherent with the present-day plate motions. Beneath the Baltic Shield, the deep asthenospheric anisotropy does not appear to be related to the present motion of the craton (Pedersen et al., 2006).

Although a two-layer model for the anisotropy, fossil in the lithosphere and oriented by the flow in the asthenosphere, seems valid under various plates, this may not apply everywhere. First, large-scale plate-motion deformation within the asthenosphere may not be present everywhere (Debayle et al., 2005) and/or may be complicated by small-scale convection in a number of regions (Maggi et al., 2006; Pedersen et al., 2006; Yuan et al., 2011). Second, although lithospheric anisotropy has been compared locally with geological trends in a number of continental areas, there is a lack of quantitative comparison, especially at global scale in oceanic regions.

In this paper, we discuss the anisotropic part of DR2012, our new global SV-wave tomographic model of the upper mantle (Debayle and Ricard, 2012). DR2012 improves upon DKP2005, our previous azimuthal anisotropy model (Debayle et al., 2005), through a larger dataset (expanded by a factor ∼ 3.7) and a new scheme that better extracts fundamental and higher-mode information. The dataset, new scheme and inversion procedure are presented in Debayle and Ricard (2012). Here, we study the agreement between fast anisotropic directions and Absolute Plate Motion (APM) or Fossil Accretion Velocity (FAV), which is recorded by the local age gradient in oceanic areas.

2. Data and tomographic inversion

Our dataset consists of $i = 374\,897$ path-average SV-wave depth dependent models (hereafter referred as "$\beta_v^i(z)$" models) obtained by waveform inversion of multimodes Rayleigh wave seismograms

(Cara and Lévêque, 1987). The waveform inversion accounts for the fundamental and up to five higher Rayleigh modes in the period range 50–250 s. It has recently been automated by Debayle and Ricard (2012).

A 3D elastic model is obtained by combining the path-average $\beta_v^i(z)$ models in a tomographic inversion. Following Lévêque et al. (1998), we invert directly for the local distribution of shear velocity and azimuthal anisotropy. For each path i with length L_i, the path average slowness $1/\beta_v^i(z)$ can be seen as the integral at each depth z of the local slowness at geographical point (θ, ϕ) and for azimuth ψ, $1/\beta_v(z, \theta, \phi, \psi)$:

$$\frac{1}{\beta_v^i(z)} = \frac{1}{L_i} \int_i \frac{1}{\beta_v(z, \theta, \phi, \psi)} \, ds \qquad (1)$$

The azimuthal variation of a long-period SV-wave propagating horizontally with velocity $\beta_v(z, \theta, \phi, \psi)$ can be approximated by:

$$\beta_v(z, \theta, \phi, \psi) = \beta_{v0}(z, \theta, \phi) + A_1(z, \theta, \phi) \cos(2\psi)$$
$$+ A_2(z, \theta, \phi) \sin(2\psi) \qquad (2)$$

The inversion is performed at each depth for the isotropic shear velocity $\beta_{v0}(z, \theta, \phi)$ and the anisotropic parameters $A_1(z, \theta, \phi)$ and $A_2(z, \theta, \phi)$. We use a tomographic scheme based on the continuous regionalization formalism of Montagner (1986), extended for the analysis of massive surface wave datasets by Debayle and Sambridge (2004). Data weighting is discussed in Debayle and Ricard (2012). At each depth, we obtain a smooth model by imposing correlations between neighboring points using a Gaussian *a priori* covariance function. This covariance function is defined by a standard deviation σ controlling the amplitude of a component of the model perturbation, and by a horizontal correlation length L, controlling the horizontal smoothness. We use standard deviations of $\sigma = 0.05$ km s^{-1} and $\sigma = 0.005$ km s^{-1} for the isotropic and anisotropic components respectively. Increasing the anisotropic standard deviation by a factor of two produces anisotropy amplitudes that can locally exceed 15%, but does not affect the pattern of anisotropic directions (Fig. A.1). Such large amplitudes predict SKS delay times of up to 8 s that exceed the largest values expected from laboratory experiments or SKS measurements (Mainprice and Silver, 1993). The same horizontal correlation length is used for both isotropic and anisotropic components.

The isotropic part of the model ($\beta_{v0}(z, \theta, \phi)$) is discussed in details in Debayle and Ricard (2012). In the present paper, we focus on the anisotropic components A_1 and A_2. Using a correlation length $L = 400$ km, we obtain the SV-wave azimuthal anisotropy maps of the upper mantle depicted in Fig. 1. Increasing L leads to smoother tomographic images with higher amplitude anomalies, but the overall pattern of anisotropic anomalies remains unchanged (Fig. A.2).

The largest azimuthal anisotropy is observed in the upper 250 km of the mantle (Fig. 1). In this depth range, azimuthal anisotropy is in general perpendicular to the ridge axis, in agreement with previous global surface wave observations (Tanimoto and Anderson, 1984; Montagner and Tanimoto, 1991; Trampert and Woodhouse, 2003; Debayle et al., 2005; Beucler and Montagner, 2006; Becker et al., 2012). Azimuthal anisotropy maps are more complex at shallow depths (the first 100 km in oceanic regions, the first 150 km in continental regions). At 200 km beneath oceanic areas, azimuthal anisotropy organizes in a smooth, large-scale pattern within the asthenosphere. At depths greater
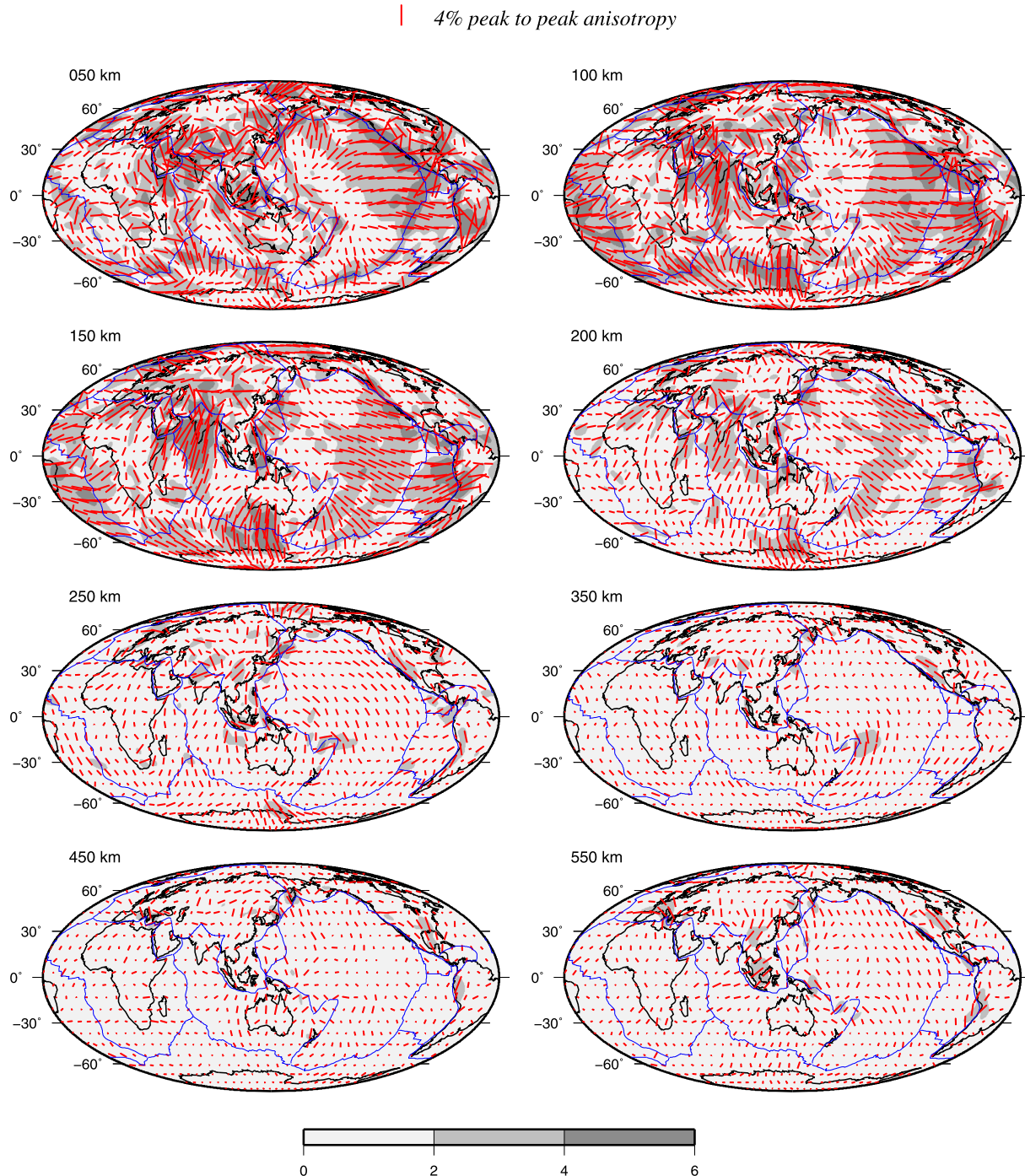
Fig. 1. SV-wave azimuthal anisotropy (red bars oriented along the axis of fast propagation) at different depths in the upper mantle. The length of the bars is proportional to the maximum amplitude of azimuthal anisotropy (bar length for 4% peak-to-peak anisotropy on top). The background grey scale indicates the amplitude of peak-to-peak azimuthal anisotropy in per cent.

than 250 km, azimuthal anisotropy is generally weak excepted in the vicinity of subductions. Within the transition zone, the largest azimuthal anisotropy correlates with the observed high seismic velocities around Indonesia and the Pacific, and in the Mediterranean region (Ritsema et al., 2011; Debayle and Ricard, 2012). This suggests some ponding of the slabs within the transition zone, producing a broad scale high velocity and deformation signature picked-up by long period surface waves.

The analysis of the anisotropy and its relation to geodynamics is presented in more details in Section 5. In Sections 3 and 4 we first assess the quality of these tomographic images.

3. Azimuthal coverage

Following Debayle and Sambridge (2004) we use "optimized Voronoi" diagrams to estimate how azimuthal anisotropy is resolved with a given ray coverage. We start from an "initial" diagram defined by a uniform 2° × 2° grid. This is justified because the shortest distance scale resolvable with long period surface wave (40–300 s) is a few hundred kilometers. From this initial diagram we built an optimized Voronoi diagram in which a specific quality criterion is satisfied for each cell. We use a quality criterion defined in Debayle and Sambridge (2004) which ensures that there

is at least a seismic path in each $36°$ bin of azimuthal coverage. This requirement of at least 5 well distributed azimuths allows the determination of the anisotropy without aliasing effects. The optimized Voronoi diagram is built using an iterative scheme where, at each step, a small fraction of the nodes which do not match the quality criterion are deleted and the Voronoi cells are recalculated from the remaining nodes. Debayle and Sambridge (2004) show that the optimized Voronoi diagram obtained with this scheme is very close to the ideal one that would contain the largest possible number of cells for which the corresponding quality criterion is satisfied.

Fig. A.3 presents a set of optimized Voronoi diagrams at different depths in the upper mantle. At each depth, they are based on the ray distribution provided by our well resolved path averaged $\beta_v^i(z)$ models, for which the *a posteriori* error is smaller than 80% of the *a priori* error (Debayle and Ricard, 2012). These diagrams provide a useful proxy for resolution. In our case, the horizontal degree of smoothing is controlled by a correlation length $L = 400$ km. A conservative choice is to consider that azimuthal anisotropy is resolved when the size of the Voronoi cells is smaller than, or comparable to the correlation surface πL^2. Fig. A.3 shows that the quality criterion is satisfied with almost no modification of the initial Voronoi diagram down to 350 km depth. In the transition zone, the size of Voronoi cells increases principally at high latitudes in the southern hemisphere, in the eastern Atlantic and Pacific oceans and in western Africa. However, the size of the Voronoi cells remain everywhere smaller or comparable to the correlation surface, which ensures that there is enough azimuthal coverage to retrieve the SV-wave azimuthal variation everywhere in the upper mantle.

4. Possible trade-offs

We performed a variety of tests to estimate the quality of our anisotropic model.

First, we verified the independence of the isotropic and anisotropic parts of our model by inverting our dataset with and without azimuthal anisotropy. As already discussed in Debayle and Ricard (2012), the isotropic velocities obtained with an isotropic inversion or with a fully anisotropic inversion are visually indistinguishable. The main difference is a slightly larger amplitude of SV-wave perturbation in the isotropic inversion by up to 2% at 150 km depth, reducing to less than 0.6% at depths greater than 200 km.

Second, we checked that the anisotropic inversion of synthetic data computed with an isotropic only model (3SMAC from Nataf and Ricard, 1995) and with the path coverage of DR2012, does not lead to a spurious anisotropy after inversion. In agreement with previous tests (Lévêque et al., 1998; Debayle and Kennett, 2000b; Maggi et al., 2006), less than 1% maximum azimuthal anisotropy is found after this inversion test.

Third, we checked that our model is not affected by the fact that Eq. (2) is approximative. This equation only considers the dominant terms of a more complex expression (see Montagner and Nataf, 1986 for a detailed discussion) and neglects the 4ψ azimuthal variation of the Rayleigh waves phase velocity. This approximation has been shown to be accurate (e.g., in Lévêque et al., 1998) and trade-off between 2ψ and 4ψ terms that was already negligible in Debayle et al. (2005) is even smaller with our present day larger dataset.

Our various test have therefore shown that the isotropic and anisotropic terms are robustly and independently recovered. The isotropic part of the velocity explains by itself 85% of the data. Taking into account the anisotropy further reduces the variance to 88% which shows that anisotropy is a second order effect. We even computed an extreme case where we inverted our data for the anisotropic component only, assuming that there was no

lateral variation in shear-wave velocity (Fig. A.4) by imposing a zero variance to the isotropic component. The data variance reduction obtained by this "purely anisotropic" inversion does not exceed 25%. This confirms the fact that the velocity perturbations are mostly isotropic. However even this extreme inversion, where the amplitude of the anisotropy exceeds 20% in some places, predicts anisotropic fabrics that remain correlated to what is obtained by the full inversion (compare Figs. 1 and A.4). This confirms that although anisotropy amplitudes are affected by the choice of the *a priori* standard deviation, the anisotropy pattern is a robust observation.

5. Results and discussion

Simple shear at the base of a moving plate produces anisotropy in olivine with a fast a-axis that follows the principal extension direction for modestly deformed olivine aggregates, and aligns with the direction of flow for large deformation (Zhang and Karato, 1995; Tommasi, 1998). Although the amplitude of Rayleigh wave azimuthal variation reduces when the a-axis depart from the horizontal, the direction of the fastest Rayleigh wave remains in the vertical plane containing the a-axis. The direction of fast SV-wave is parallel to the direction of fast Rayleigh wave (Babuška and Cara, 1991), and therefore parallel to the a-axis of olivine crystals. Although complications can occur under water rich conditions (Jung and Karato, 2001; Kaminski, 2002) or due to the presence of other anisotropic upper mantle minerals such as pyroxene (Beghein and Trampert, 2004), we interpret our fast SV-wave anisotropic directions in terms of olivine a-axis orientation, and then in terms of fossil (fabrics) or present shear strain responsible for crystal orientation.

Fig. 2(a) displays the percentage of peak-to-peak azimuthal anisotropy across an age-dependent average cross-section in DR2012. Significant azimuthal anisotropy ($> 1\%$) is found down to ~ 250 km depth. The strongest azimuthal anisotropy is found in the lithosphere (< 200 km) of continental regions and within the asthenosphere of oceanic regions. The largest oceanic anisotropy is observed within the asthenosphere, at ages younger than 50 Ma. The asthenospheric anisotropic layer deepens progressively with age and follows the trend predicted by the square root of age cooling model (Turcotte and Schubert, 2002). The isotherm that corresponds to the base of the thermal boundary layer ($T = 1100°C$ solid line) roughly delineates the top of the strongly anisotropic region. Finally, a striking feature of Fig. 2(a) is the fact that on average, the depth range where significant azimuthal anisotropy ($> 1\%$) is observed, does not differ between continents and oceans. We argue that this cannot be attributed to the choice of standard deviations for the isotropic and anisotropic components. Using a larger standard deviation value for anisotropy leads to unrealistic anisotropy amplitudes at depths shallower than 200 km (Fig. A.1), but does not introduce a difference in the depth extent of anisotropy between oceans and continents. Note also that our damping is uniform with depth (the *a priori* standard deviations are independent of depth) and cannot be responsible for the observed decrease of anisotropy with depth. As Fig. A.3 ensures that there is no significant change of our azimuthal coverage down to 350 km depth, we are confident in our observation that there is no ocean/continent difference in the depth extent of azimuthal anisotropy. This contrasts with previous results by Gung et al. (2003), who suggested an anisotropic layer overlain by a Lehman discontinuity under continents (near 200–250 km depth) and overlain by a Gutenberg discontinuity under oceans (near 60–80 km depth).

In order to search for a possible relation between the anisotropy strength and the surface plate velocity, we separate in Figs. 2(b), (c), the 6 fastest-moving plates (panel b) and the other plates
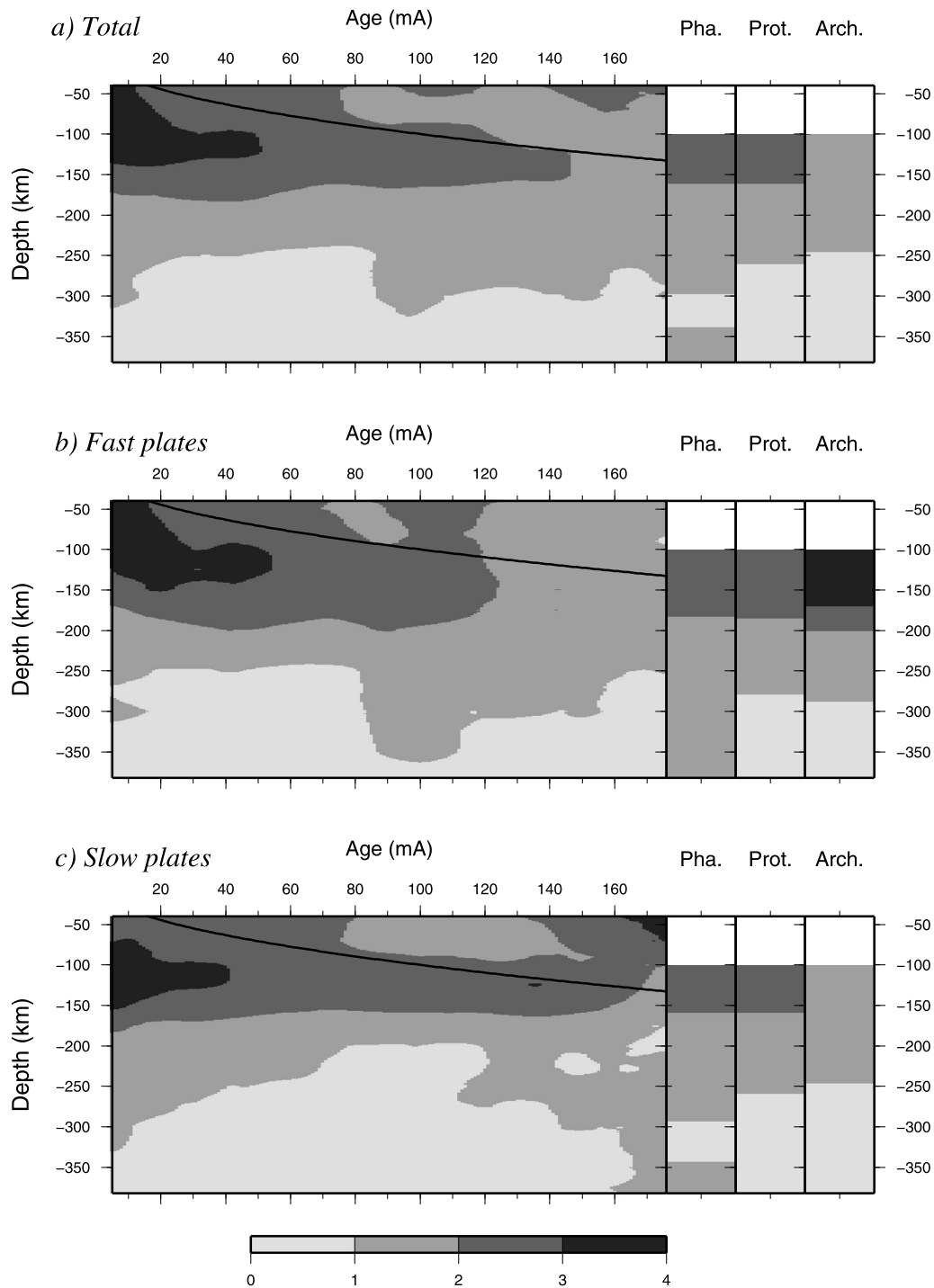
Fig. 2. Peak-to-peak azimuthal anisotropy as a function of age and depth, over oceanic regions and continents (Phanerozoic, Pha., Proterozoic, Prot., and Archean, Arch.). The anisotropy is averaged (a) globally; (b) for 6 fastest-moving plates; (c) for the other plates. For oceanic regions, a continuous image was created by averaging each parameter along the Müller et al. (2008) isochrons, using a sliding window of ±5 Ma. The continuous black lines indicate the position of the thermal boundary layer for the half-space cooling model (Turcotte and Schubert, 2002). Continental provinces are defined according to 3SMAC (Nataf and Ricard, 1995). Continental profiles are only shown at depths greater or equal to 100 km, where the effect of crustal correction is negligible (Debayle and Ricard, 2012).

(panel c). Although faster plates display a stronger anisotropy within the Archean lithosphere (namely, beneath Australia and India), the main features of Fig. 2(a) are preserved. The depth extent of azimuthal anisotropy is roughly similar for fast and slow-moving plates, and there are no major differences in the strength of anisotropy beneath oceanic regions.

In the following, we compare our fast anisotropy maps with current plate motions and fossil accretion velocities corresponding to the end-member models commonly accepted for the origin of upper mantle anisotropy.

The current velocities are taken from the absolute plate motion (APM) model NUVEL-1A of DeMets et al. (1994) expressed in a no-net reference frame (Fig. 3(a)). We are aware that some global rotation must be present between the average lithospheric velocity and the underlying model (Ricard et al., 1991). The amplitude of this motion is uncertain but its rotation axis is better constrained.
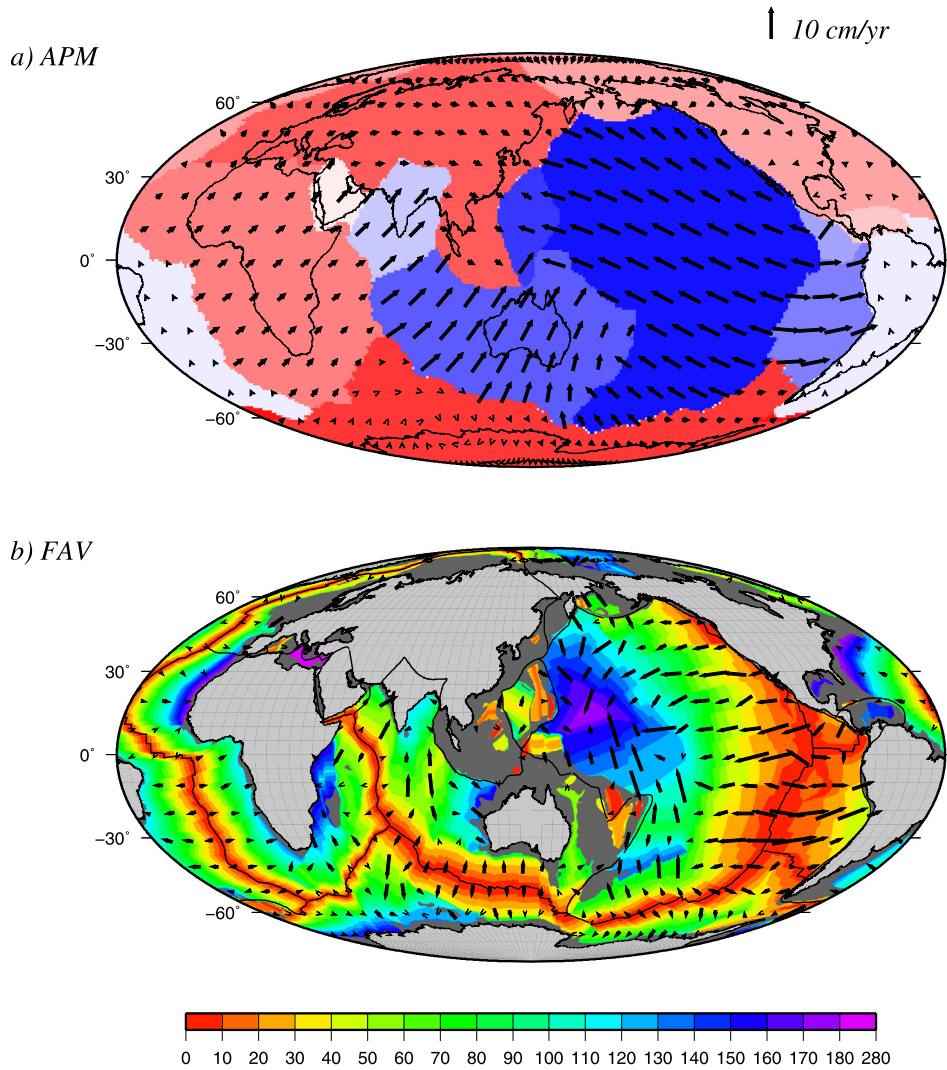
Fig. 3. (a) Tectonic plates and actual plate motion (APM), according to the NUVEL-1A model (DeMets et al., 1994). Black bars indicate APM directions. Their length is proportional to the actual plate velocities. A red via white to blue color scale is used to differentiate tectonic plates from the slowest to the fastest. We consider India, Coco, Nazca, Australia, Philippine Sea, Pacific shown in purple to blue as "fast-moving". (b) Seafloor age and fossil accretion velocity (FAV). Color scale indicate seafloor age after Müller et al. (2008). FAV is obtained in oceanic regions by computing the gradient of seafloor age. Black bars indicate FAV directions. Their lengths are proportional to the fossil accretion velocities.

We therefore added to the no-net rotation model NUVEL-1A a proportion $0 \leqslant \epsilon \leqslant 1$ of the global rotation included in HS2-NUVEL1 (Gripp and Gordon, 1990). We found that NUVEL-1A (i.e., $\epsilon = 0$) slightly better correlates with our anisotropic maps than models with a non-zero global lithospheric velocity (i.e., models with $\epsilon \neq 0$). At any rate, the conclusions of this paper are qualitatively identical for all plate motion models between NUVEL-1A and HS2-NUVEL1.

The fossil accretion velocity is the direction of seafloor spreading $\mathbf{v}(\mathbf{x}, \mathrm{age}(\mathbf{x}))$, recorded at age($\mathbf{x}$) when the lithosphere was formed, in the lithosphere presently at position $\mathbf{x}$. This velocity can be retrieved from the present-day seafloor ages by considering two points on the seafloor separated by their formation ages, t and $t + \delta t$ and their positions $\mathbf{x}$ and $\mathbf{x} + \delta \mathbf{x}$. We can define the age gradient $\nabla \mathrm{age}$ by $\delta t = \nabla \mathrm{age} \cdot \delta \mathbf{x}$. The vector $\delta \mathbf{x}$ projected onto the fossil seafloor spreading velocity $\delta \mathbf{v}$, i.e., $\mathbf{v} \cdot \delta \mathbf{x} / \|\mathbf{v}\|$ is just the width $\|\mathbf{v}\| \delta t$ that has been accreted to the plate between t and $t + \delta t$. One has thus $\delta t = \nabla \mathrm{age} \cdot \delta \mathbf{x} = \mathbf{v} \cdot \delta \mathbf{x} / \|\mathbf{v}\|^2$. This proves that the gradient of seafloor age is related to the fossil spreading velocity by $\nabla \mathrm{age} = \mathbf{v} / \|\mathbf{v}\|^2$. From this equation, we deduce that $\|\nabla \mathrm{age}\| = 1/\|\mathbf{v}\|$ and that the fossil accretion velocity (FAV) is:

$$\mathbf{v} = \frac{\nabla \mathrm{age}}{\|\nabla \mathrm{age}\|^2} \tag{3}$$

This fossil accretion velocity FAV is displayed in Fig. 3(b). The FAV provides a basis to quantify the agreement between anisotropy and fossil directions in oceanic regions. We did not estimate a fossil formation velocity for continents, because their complex tectonic history makes this task impossible. Over young oceanic plates, APM and FAV are rather similar but FAV directions are more perpendicular to the ridges than the APM. At old ages (mostly older than 50 Ma which corresponds to the drastic change in the Pacific plate motion as recorded in the Hawaiian-Emperor bend; Sharp and Clague, 2006; Whittaker et al., 2007), the APM and FAV directions can be very different. This is particularly true in the old Pacific plate, between South Africa and Antarctica or between Australia and Sumatra.

In Figs. 4 and 5, we map the agreement between fast anisotropic directions and APM at different depths in the upper mantle. We use the parameter $A\cos(2\alpha)$, where A is the amplitude of anisotropy and α the angle between APM and fast anisotropic directions ($0° \leqslant \alpha \leqslant 90°$). The left columns of Figs. 4 and 5 display maps of $A\cos(2\alpha)$ for the 6 fastest plates (plate velocity larger
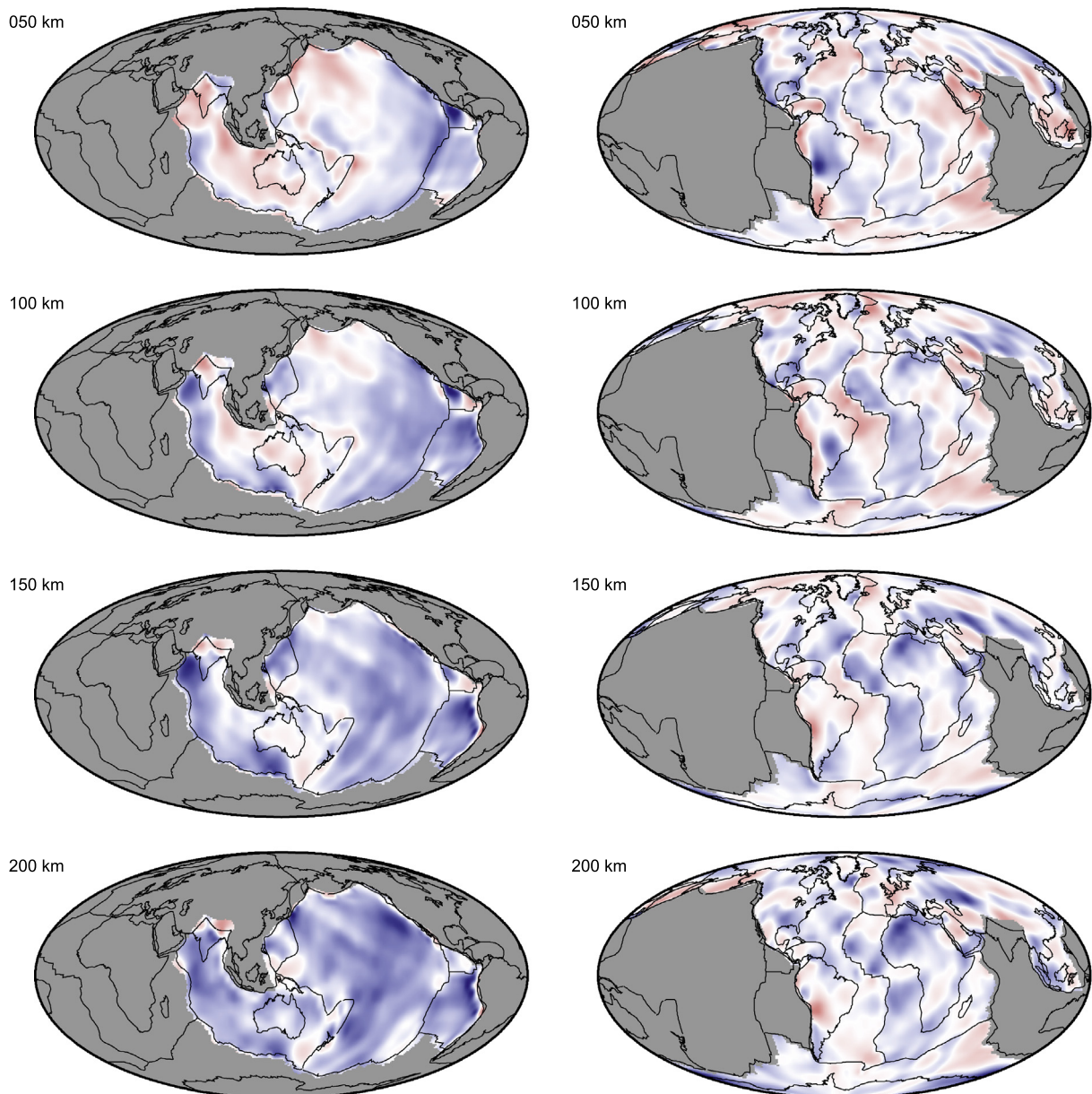
Fig. 4. Agreement between fast direction of SV waves and APM according to the NUVEL-1A model (DeMets et al., 1994). The agreement is shown separately for fast-moving (left column) and slow-moving plates (right column). The parameter $A\cos(2\alpha)$, where A is the amplitude of the fast SV-wave vector and α the angle between APM and fast SV-wave azimuth, is shown. Good agreement (parallelism of the two vectors) is represented in blue, weak agreement in white and bad agreement (orthogonality) in red. The color scales are symmetric, adapted to cover the full range of values at each depth, the zero value corresponds in some case to a zero anisotropy or more often to an angle of 45° between fast anisotropy and APM.

than 4 cm yr^{-1}, India, Coco, Nazca, Australia, Philippine Sea and Pacific) shown in purple to blue in Fig. 3(a). The right columns of Figs. 4 and 5 display the same parameter for the slower plates.

For the 6 fastest plates (left columns of Figs. 4 and 5), fast anisotropic directions and APM agree at large scale in the up-permost 250 km (very similar maps are obtained using a plate model that includes a global rotation). At 50 km depth, this agree-ment is restricted to young oceanic regions, where the litho-sphere is thin. In the Pacific ocean, the transition occurs near the 50 Ma isochron which marks the approximate age at which major plate re-organization occurred (Sharp and Clague, 2006; Whittaker et al., 2007). At 100 and 150 km depth, the agree-ment extends to old oceanic basins, suggesting that the depth of plate-motion-induced deformation increases with the age of the seafloor and the thickness of the oceanic lithosphere. Continental anisotropy is consistent with APM between 100 and 200 km for

India and at depths larger than 150 km for Australia. At 150 and 200 km depths, the region where anisotropy agrees with APM cov-ers almost entirely the 6 fastest tectonic plates. This large-scale pattern is still present at 250 km depth, although the agreement vanishes in some regions (e.g., western Australia or Philippine sea). At depths greater than 250 km, the pattern disorganizes (Fig. 5).

The right columns of Figs. 4 and 5 display the APM/anisotropy correlation for the slower plates. Fast anisotropic directions and APM sometimes agree over broad regions, but these regions never cover entirely a tectonic plate. This poor overall correlation re-mains when a plate motion model including a global rotation is used, although the details of the maps may change.

These results clearly suggest two different regimes of astheno-spheric flow. Beneath the 6 fastest plates, plate motion orga-nizes the large-scale pattern of asthenospheric anisotropy. Beneath slower plates, plate motion only partly controls the asthenospheric
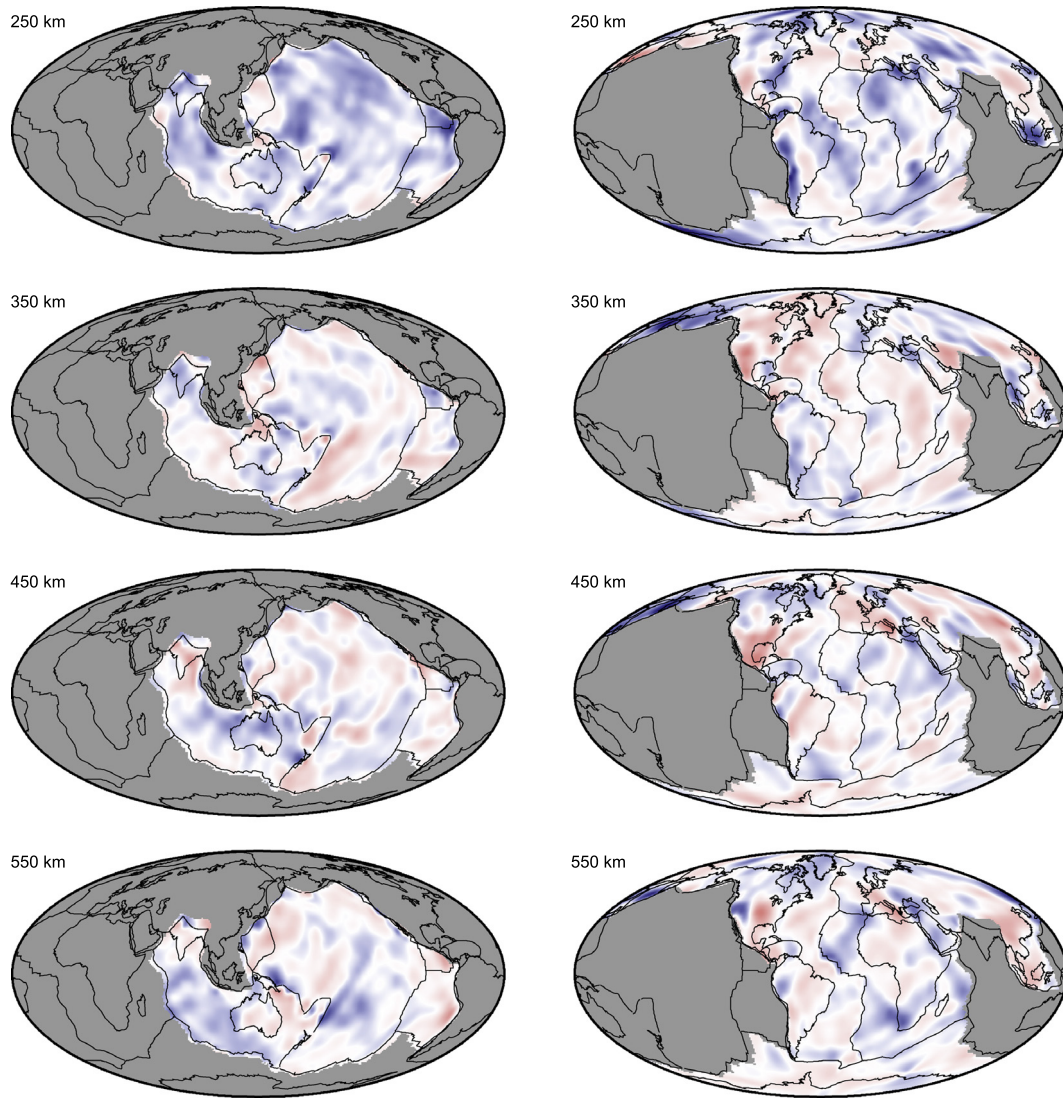
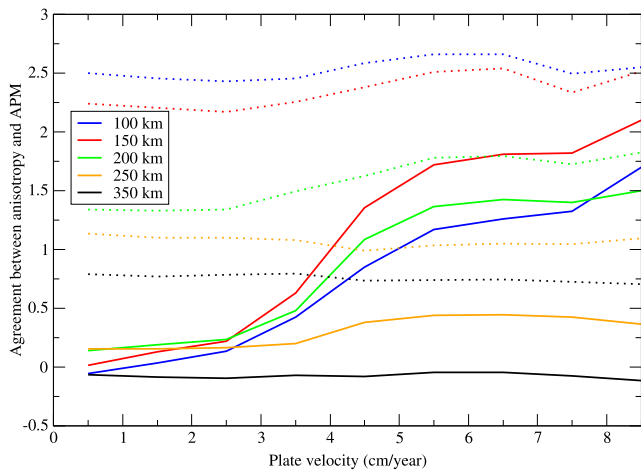**Fig. 5.** Same as Fig. 4 but for deeper depths between 250 and 550 km.

Fig. 6. The anisotropy along the APM, $\langle A\cos(2\alpha)\rangle$ is plotted as a function of plate velocity (solid lines) for different depths in the upper mantle (A is peak-to-peak anisotropy in percent, α is the angle between APM and fast SV azimuth, $A\cos(2\alpha)$ is averaged for all geographical points with similar plate velocities, using a sliding window of ± 2 cm yr^{-1} width). Dotted lines show the peak-to-peak anisotropy strength $\langle A \rangle$ as a function of plate velocities. Comparison of the dashed and continuous lines at a given depth indicates the maximum proportion of anisotropy which is parallel to APM.

flow which is presumably affected by secondary convection. This result is confirmed in Fig. 6 which displays the average quantities $\langle A\cos(2\alpha)\rangle$ and $\langle A\rangle$ as a function of plate velocity for different depths in the upper mantle (we average the anisotropies for all the points having the same velocity within ± 2 cm yr^{-1}). The average anisotropy ($\langle A\rangle$, dotted lines) and the average anisotropy aligned with plate motions ($\langle A\cos(2\alpha)\rangle$, solid lines) have very different behaviors. The average anisotropy appears independent of plate velocity and simply decreases with depth from 2.5% around 100 km. On the contrary, the aligned anisotropy is maximum around 150–200 km depth. In the depth range between 100 and 250 km, corresponding to the oceanic asthenosphere, a clear change in the $\langle A\cos(2\alpha)\rangle$ curves occurs at velocities of about 4 cm yr^{-1}. Regions with plate velocities greater than 4 cm yr^{-1} have up to 80% of their anisotropy (compare the solid and dotted lines) which is aligned with the plate motion. Regions with plate velocities smaller than 3 cm yr^{-1} have either a very small anisotropy (A small) or this anisotropy is not correlated with APM (α close to 45°). Fig. 6 also shows that the alignment of the anisotropy saturates rapidly with the velocity; the anisotropy is not much larger at 8 cm yr^{-1} than at 5 cm yr^{-1}. One may speculate that the maximum of crystal orientations is rapidly reached and that a further increase in velocity and strain does not lead to a larger anisotropy.
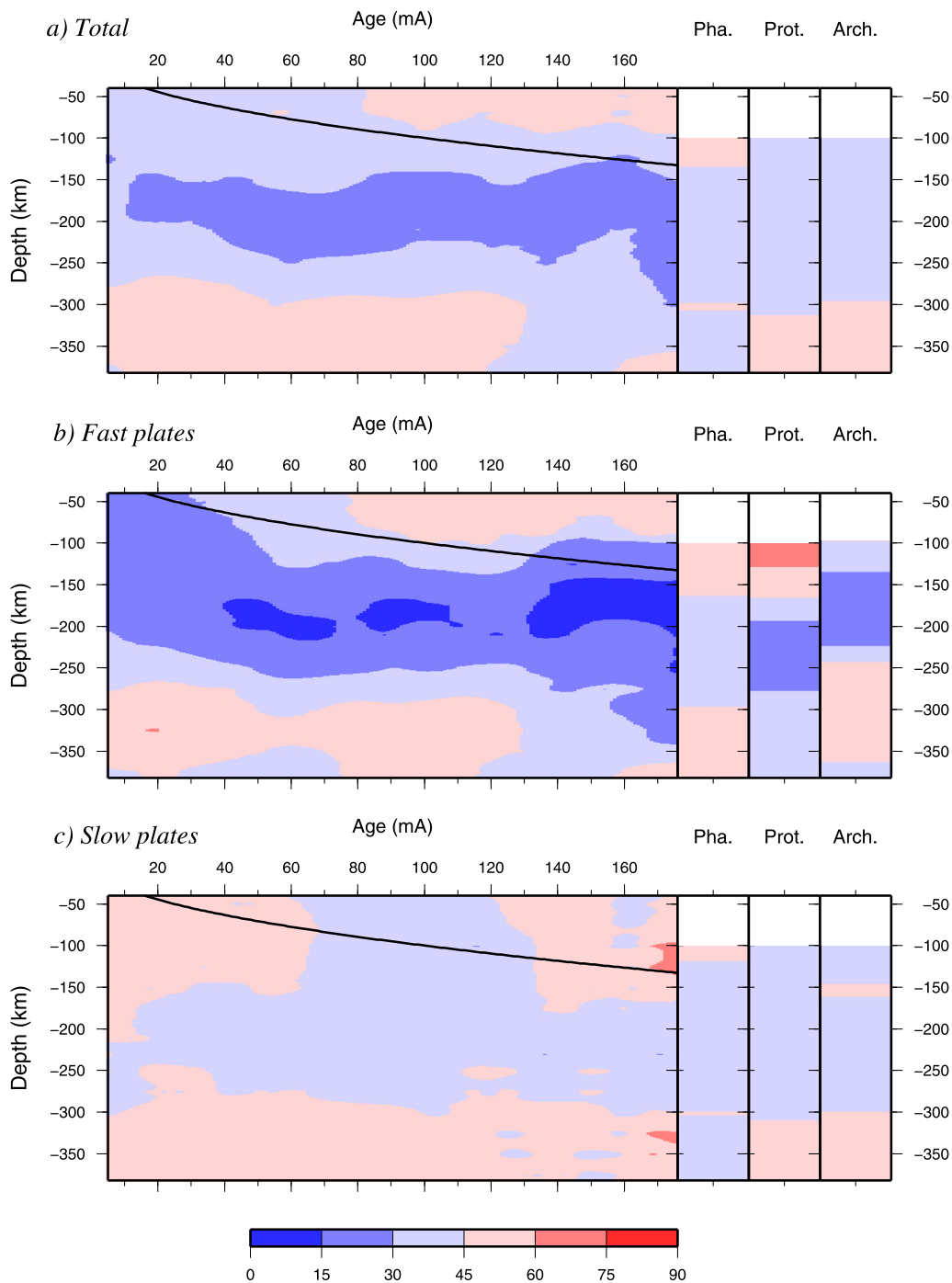
Fig. 7. Cross-sections with respect to age of the angular difference between fast anisotropic directions and APM (panel (a) global average, panel (b), fast plates, panel (c), slow plates). Continental plates are divided into Phanerozoic (labelled Pha.), Proterozoic (labelled Prot.) and Archean (labelled Arch.). Under the lithosphere defined by solid lines, the anisotropy is closely aligned with APM for fast-moving plates only.

In Fig. 7, we plot age-dependent cross-sections of the angular difference between fast anisotropic and APM directions. The angular difference α is defined between 0 and 90°. This quantity is averaged globally (Fig. 7(a)), for the six fastest plates (Fig. 7(b)), and for the remaining plates (Fig. 7(c)). A remarkable feature of Figs. 7(a), (b) is the progressive deepening of the layer where plate motion controls the anisotropy. This deepening follows approximately the trend predicted by the square root of age cooling model (Turcotte and Schubert, 2002), as observed for the SV-velocity in our recent seismic models (Maggi et al., 2006; Debayle and Ricard, 2012). This layer extends to a depth of 250–300 km and is clearly due to fast-moving plates (Fig. 7(b)) which imprint the

global average. In contrast, the asthenosphere is not dominated by plate motion parallel anisotropy beneath slow-moving plate (Fig. 7(c)). This suggests that slow-moving plates do not control the large scale pattern of asthenospheric anisotropy. Finally, it is worth noting that within most of the oceanic lithosphere, between the surface and the isotherm depicted by the solid line ($T < 1100\,°C$), anisotropy and APM do not agree. For seafloor ages greater than 80 Ma, the average angle between fast anisotropy and APM is larger than 45° in the lithosphere (Fig. 7(a)).

The continental profiles of Fig. 7 suggest that anisotropy beneath Australia and India, which are the only continents on the 6 fastest plates, better align with APM than anisotropy beneath
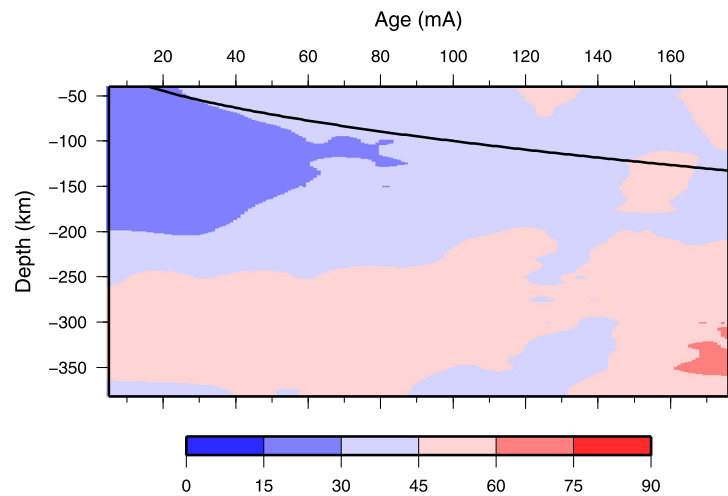
Fig. 8. Same as Fig. 7 but for the angular difference between fast anisotropic directions and FAV. Note that in this case, the angular difference is a global average, as we did not separate plates depending on the amplitude of their fossil accretion rate. In the lithosphere, the correlation with anisotropy is better with FAV than with APM.

other continents. This reflects the fact that plate-motion controls only partly the asthenospheric flow of slow-moving plates, with a large portion of continents showing no agreement with APM.

In Fig. 8, we now plot the age-dependent cross-section of the angular difference between fast anisotropic directions and the fossil accretion directions. For ages younger than 60 Ma, we observe an angular difference smaller than 30°. This is even better than what is found with the APM directions (compare with Fig. 7(a)). For ages younger than 60 Ma, FAV and APM directions are rather close, but FAV is, by construction, perpendicular to the ridges while this is not everywhere the case for the APM. A striking feature of Fig. 8, is that the region where anisotropy is consistent with FAV, at least to some extent, covers almost entirely the oceanic lithosphere. Although the angular difference remains quite large (between 30° and 45°), such a positive correlation was only observed at ages younger than 80 Ma in the case of the APM (compare Fig. 8 with Fig. 7(a)). This agreement is modest but seems meaningful. Two effects make indeed the exercise of correlating anisotropy to FAV difficult. First, the fossil accretion directions show rapid changes, second, the fossil directions are likely imprinted in the shallowest layers only. A shallow and rapidly variable anisotropy is difficult to recover due to the necessary damping of the inversion. The fact that for all ages, the shallow oceanic anisotropy better correlates with FAV than with APM confirms the existence of frozen-in anisotropy near the surface.

In order to investigate in more details where anisotropy agrees with APM or FAV, we plot in Fig. 9 the angular differences at different depths in the upper mantle. We use a very simple classification: in dark blue where fast anisotropy matches both APM and FAV, in light blue, where fast anisotropy matches APM only, in green where fast anisotropy matches FAV only, in orange where fast anisotropy matches neither APM nor FAV (the classes are defined by an angle lower or larger than 30°). At depths greater than 250 km, the anisotropy pattern agrees neither with APM nor with FAV for most oceanic areas (orange). At depths shallower than 250 km, anisotropy agrees with both APM and FAV beneath young seafloor, where the APM and FAV directions are close (dark blue). At 50 km depth, the green region, where anisotropy agree with FAV but not APM covers most old oceanic basins (notice in particular the old Pacific, the South Africa–Antarctica region, west of Australia...). As depth increases from 50 to 200 km, the area covered by this region reduces beneath the 6 fastest plates, and is progressively replaced by the light blue region, where anisotropy correlates with APM but not FAV. Fig. 9 clearly confirms the existence of a two-layer anisotropic model in oceanic areas for the 6

fastest plates. In the upper layer, anisotropy is related to frozen-in deformation within the lithosphere, while in the deeper layer, anisotropy is related to plate-motion active deformation within the asthenosphere. The transition between these two layers deepens with the square root of seafloor age and the olivine crystal orientation freezes below a temperature of about 1100 °C.

It is interesting to compare our observations with models of anisotropy under oceanic plates (Ribe, 1989; Kaminski and Ribe, 2002; Kaminski et al., 2004) (keeping in mind, however, that our model only captures the horizontal component of anisotropy). For example Fig. 6 of Kaminski et al. (2004) computes the anisotropy under a permanent ridge, for an aggregate (olivine + pyroxene) that should represent a typical pyrolite composition. This model does not predict a horizontal anisotropy just beneath the ridge (the fast axis should there, be rather vertical than horizontal). However within a few 10 km, the anisotropy is predicted to become close to horizontal. With a tomographic inversion where the horizontal correlation length is 400 km, it is not surprising that we cannot capture a probable minimum of horizontal anisotropy beneath ridges. The anisotropy predicted by the geodynamic model of Kaminski et al. (2004) seems also to be rapidly uniform in the asthenosphere and the lithosphere. In the asthenosphere, this is in agreement with our tomographic model under fast plates (Fig. 6) although the observed amplitude (about 1.5% at 150 km depth) seems lower than what is predicted by simulations. Under slow plates, we do not observe a clear anisotropy related to the plate motion: the flow at depth is probably more complex than a forced flow driven by surface motion. The case of frozen-in anisotropy, which is only visible when a plate changes direction has not been considered in the geodynamic simulations of Kaminski et al. (2004). The slight decrease of the anisotropy amplitude with distance (Fig. 2) may indicate that the peridotite grains forget the anisotropy that they acquired during the strong straining near the ridge, for example by a process of normal grain growth (Ricard and Bercovici, 2009).

6. Conclusion

The observations support the hypothesis that upper mantle anisotropy is caused principally by the preferential orientation of olivine crystals along the flow. Globally, the anisotropy amplitude decreases with depth and does not show a significant difference of amplitude beneath oceans or continents (Fig. 2).

Under oceans, the anisotropy strength is on average moderate (< 2%) in the lithosphere and slightly stronger (> 2%) in the asthenosphere. We find that a two-layers model, with shallow
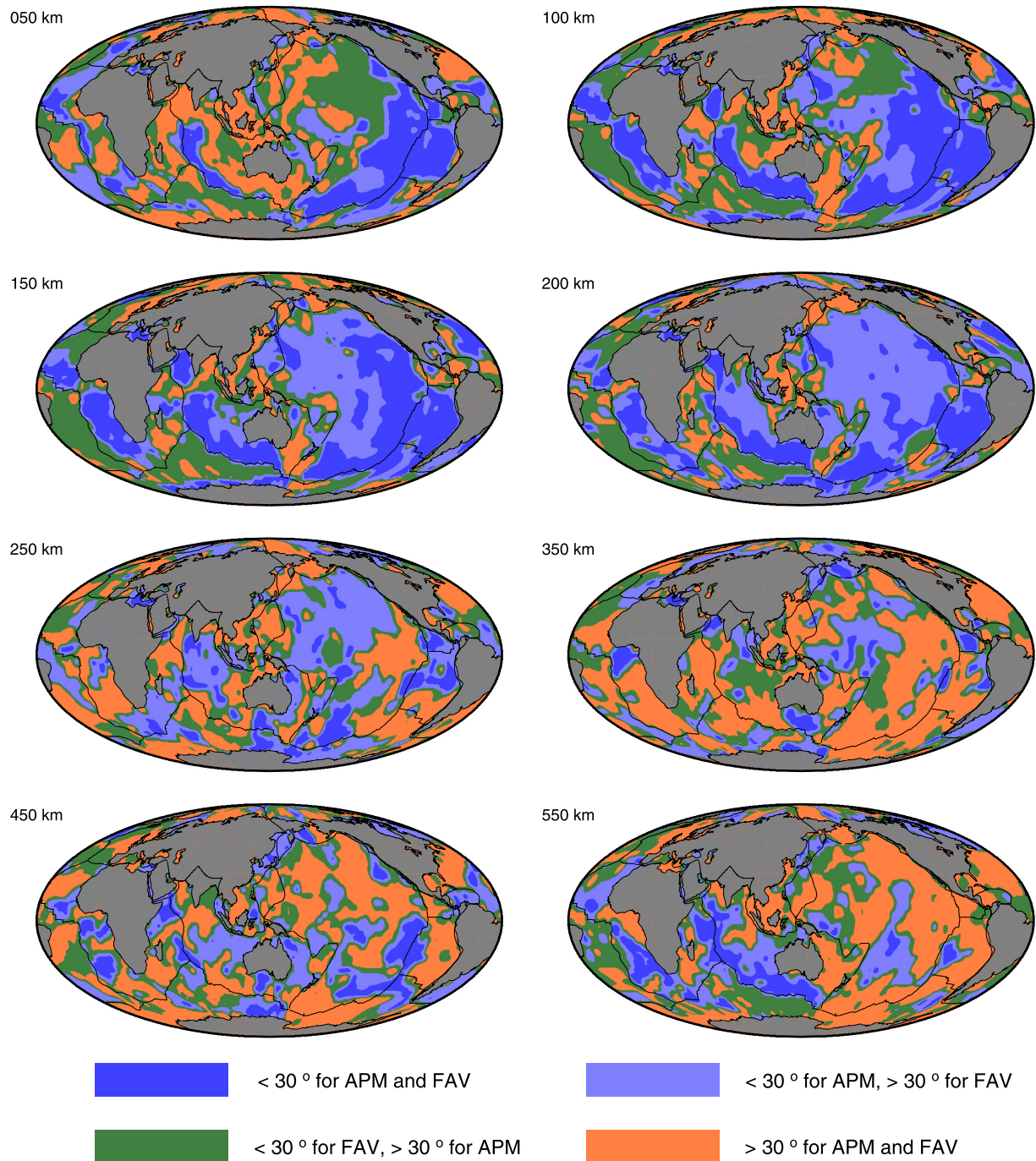
Fig. 9. Angular difference between fast direction of SV waves, APM and FAV directions. Although in the asthenosphere the anisotropy is well correlated with APM (dark or light blue), in the lithosphere, the correlation is better with the FAV (green or dark blue).

anisotropy frozen-in within the lithosphere and deeper anisotropy related to present-day plate-motion deformation within the asthenosphere, is in agreement with the observations for the six fastest-moving plates. For these plates, azimuthal anisotropy generally correlates with FAV within the oceanic lithosphere, and correlates with APM in the asthenosphere. The transition between frozen-in and flow-induced anisotropy follows the isotherm classically defining the lithosphere around 1100 °C. The amplitude of the anisotropy increases with the plate velocity but saturates for velocities larger than around 5 cm yr^{-1} (Fig. 6). In the asthenosphere, between 150 and 200 km depth, the correlation between anisotropy and APM is striking (Fig. 9).

The situation is more complex beneath slow-moving plates. Fast anisotropic directions and APM or FAV sometimes agree over broad regions. Such large-scale agreement has previously been observed, for example in central and eastern North America, where SKS fast axes are generally parallel with APM expressed in a hot-spot reference frame (Fouch et al., 2000; Wang et al., 2008), although lithospheric anisotropy appears also to be required (Barruol et al., 1997; Fouch et al., 2000). However, from our global model, these regions never entirely cover a tectonic plate and the average aligned anisotropy remains very small (Fig. 6). This suggests that under slow-moving plates, the convective flow is more affected by the secondary convection than organized by the surface motion.

A typical mantle velocity of around 4 cm yr^{-1}, independent of plate motion, would explain that only plates moving faster than that can imprint the anisotropic pattern. This ubiquitous flow, independent of plate motion, would also explain why the total anisotropy is more or less uniform in the asthenosphere and even slightly larger under the low viscosity young oceans (Fig. 2). The details of the correlation between anisotropy and slow-moving plates depend however of the chosen plate velocity model (no-net rotation versus hot-spot reference frame). We found unfortunately no global lithospheric rotation that improves significantly the overall correlation between anisotropy and slow-moving plates.

The two continents located on the six fastest-moving plates, India and Australia, have the strongest azimuthal anisotropy and display the best agreement with APM. The asthenospheric layer is located below 100 km for India and below 150 km for Australia. This is in good agreement with previous regional (Lévêque et al., 1998; Debayle and Kennett, 2000b, 2000a) global studies (Debayle et al., 2005) and not much deeper than the asthenosphere under oceans. There is no indication of continental-scale alignment of anisotropy with velocity under the other continents although some authors have suggested that a two-layer model, with a deeper asthenospheric layer beneath continents, applies at global scale (Gung et al., 2003).

We conclude that the six fastest-moving plates are the only ones that produce sufficient shearing at their base to organize the asthenospheric anisotropy at the scale of the entire tectonic plates. Beneath slower plates, the convection flow is only partly controlled by plate motions, and small-scale convection disturbs an otherwise simpler pattern of anisotropy. Finally, we do not observe a clear ocean/continent difference in the depth extent of azimuthal anisotropy, in contrast with previous observations based on radial anisotropy (Gung et al., 2003).

Acknowledgements

Appendix A. Supplementary material

Supplementary material related to this article can be found online at http://dx.doi.org/10.1016/j.epsl.2013.06.025.

References

Adam, J.M., Lebedev, S., 2012. Azimuthal anisotropy beneath southern Africa from very broad-band surface-wave dispersion measurements. Geophys. J. Int. 191 (1), 155–174.

Aki, K., Kanimura, K., 1963. Phase velocity of Love waves in Japan (Part 1): Love waves from the Aleutian shock of march 1957. Bull. Earthq. Res. Inst. 41, 243–259.

Babuška, V., Cara, M., 1991. Seismic Anisotropy in the Earth. Kluwer Acad., Norwell, Mass.

Barruol, G., Silver, P.G., Vauchez, A., 1997. Seismic anisotropy in the eastern United States: deep structure of a complex continental plate. J. Geophys. Res. 102, 8329–8348.

Becker, T.W., Ekstroem, G., Boschi, L., Woodhouse, J.H., 2007. Length scales, patterns and origin of azimuthal seismic anisotropy in the upper mantle as mapped by Rayleigh waves. Geophys. J. Int. 171 (1), 451–462.

Becker, T.W., Lebedev, S., Long, M.D., 2012. On the relationship between azimuthal anisotropy from shear wave splitting and surface wave tomography. J. Geophys. Res. 117, B01306. http://dx.doi.org/10.1029/2011JB008705.

Beghein, C., Trampert, J., 2004. Probability density functions for radial anisotropy: implications for the upper 1200 km of the mantle. Earth Planet. Sci. Lett. 217 (1–2), 151–162.

Beucler, E., Montagner, J., 2006. Computation of large anisotropic seismic heterogeneities (CLASH). Geophys. J. Int. 165 (2), 447–468.

Beucler, E., Stutzmann, E., Montagner, J., 2003. Surface wave higher-mode phase velocity measurements using a roller-coaster-type algorithm. Geophys. J. Int. 155 (1), 289–307.

Cara, M., Lévêque, J., 1987. Waveform inversion using secondary observables. Geophys. Res. Lett. 14, 1046–1049.

Debayle, E., 1999. SV-wave azimuthal anisotropy in the Australian upper mantle: preliminary results from automated Rayleigh waveform inversion. Geophys. J. Int. 137 (3), 747–754.

Debayle, E., Kennett, B., 2000a. Anisotropy in the Australasian upper mantle from Love and Rayleigh waveform inversion. Earth Planet. Sci. Lett. 184 (1), 339–351.

Debayle, E., Kennett, B., 2000b. The Australian continental upper mantle: structure and deformation inferred from surface waves. J. Geophys. Res. 105 (B11), 25423–25450.

Debayle, E., Ricard, Y., 2012. A global shear velocity model of the upper mantle from fundamental and higher Rayleigh mode measurements. J. Geophys. Res. 117, B10308. http://dx.doi.org/10.1029/2012JB009288.

Debayle, E., Sambridge, M., 2004. Inversion of massive surface wave data sets: model construction and resolution assessment. J. Geophys. Res. 109, B02316. http://dx.doi.org/10.1029/2003JB002652.

Debayle, E., Kennett, B., Priestley, K., 2005. Global azimuthal seismic anisotropy and the unique plate-motion deformation of Australia. Nature 433 (7025), 509–512.

DeMets, C., Gordon, R., Argus, D., Stein, S., 1994. Effect of recent revisions to the geomagnetic reversal time-scale on estimates of current plate motions. Geophys. Res. Lett. 21 (20), 2191–2194.

Ekstrom, G., 2011. A global model of Love and Rayleigh surface wave dispersion and anisotropy, 25-250 s. Geophys. J. Int. 187 (3), 1668–1686.

Forsyth, D., 1975. The early structural evolution and anisotropy of the oceanic upper mantle. Geophys. J. R. Astron. Soc. 43, 103–162.

Fouch, M., Fischer, K., Parmentier, E., Wysession, M., Clarke, T., 2000. Shear wave splitting, continental keels, and patterns of mantle flow. J. Geophys. Res. 105 (B3), 6255–6275.

Gripp, A.E., Gordon, R.G., 1990. Current plate velocities relative to the hotspots incorporating the NUVEL-1 global plate motion model. Geophys. Res. Lett. 17 (8), 1109–1112.

Gung, Y., Panning, M., Romanowicz, B., 2003. Global anisotropy and the thickness of continents. Nature 422 (6933), 707–711.

Hess, H., 1964. Seismic anisotropy of uppermost mantle under oceans. Nature 203 (494), 629–631.

Jung, H., Karato, S., 2001. Water-induced fabric transitions in olivine. Science 293 (5534), 1460–1463.

Kaminski, E., 2002. The influence of water on the development of lattice preferred orientation in olivine aggregates. Geophys. Res. Lett. 29 (12). http://dx.doi.org/10.1029/2002GL014710.

Kaminski, E., Ribe, N., 2002. Timescales for the evolution of seismic anisotropy in mantle flow. Geochem. Geophys. Geosyst. 3. http://dx.doi.org/10.1029/2001GC000222.

Kaminski, E., Ribe, N., Browaeys, J., 2004. D-Rex, a program for calculation of seismic anisotropy due to crystal lattice preferred orientation in the convective upper mantle. Geophys. J. Int. 158 (2), 744–752.

Lebedev, S., van der Hilst, R.D., 2008. Global upper-mantle tomography with the automated multimode inversion of surface and S-wave forms. Geophys. J. Int. 173 (2), 505–518.

Lebedev, S., Nolet, G., Meier, T., van der Hilst, R., Masters, G., 2005. Automated multimode inversion of surface and S waveforms. Geophys. J. Int. 162 (3), 951–964.

Lévêque, J.J., Cara, M., 1983. Long-period Love wave overtone data in North-America and the Pacific-Ocean – New evidence for upper mantle anisotropy. Phys. Earth Planet. Inter. 33 (3), 164–179.

Lévêque, J.J., Debayle, E., Maupin, V., 1998. Anisotropy in the Indian Ocean upper mantle from Rayleigh and Love waveform inversion. Geophys. J. Int. 133 (3), 529–540.

Long, M.D., Becker, T.W., 2010. Mantle dynamics and seismic anisotropy. Earth Planet. Sci. Lett. 297 (3–4), 341–354.

Maggi, A., Debayle, E., Priestley, K., Barruol, G., 2006. Azimuthal anisotropy of the Pacific region. Earth Planet. Sci. Lett. 250 (1–2), 53–71.

Mainprice, D., Silver, P.G., 1993. Interpretation of SKS-waves using samples from the subcontinental lithosphere. Phys. Earth Planet. Inter. 78, 257–280.

Marone, F., Romanowicz, B., 2007. The depth distribution of azimuthal anisotropy in the continental upper mantle. Nature 447 (7141), 198–201.

McEvilly, T., 1964. Central U.S. crust upper-mantle structure from Love and Rayleigh wave phase velocity inversion. Bull. Seismol. Soc. Am. 54, 1997–2016.

Montagner, J., 1986. Regional three-dimensional structures using long-period surface waves. Ann. Geophys. 4, 283–294.

Montagner, J., Nataf, H., 1986. A simple method for inverting the azimuthal anisotropy of surface waves. J. Geophys. Res. 91, 511–520.

Montagner, J., Tanimoto, T., 1991. Global upper mantle tomography of seismic velocities and anisotropies. J. Geophys. Res. 96, 20337–20351.

Müller, R., Sdrolias, M., Gaina, C., Roest, W., 2008. Age, spreading rates and spreading symmetry of the world's ocean crust. Geochem. Geophys. Geosyst. 9, Q04006.

Nataf, H., Ricard, Y., 1995. 3SMAC: an a priori tomographic model of the upper mantle based on geophysical modeling. Phys. Earth Planet. Inter. 95, 101–122.

Nataf, H., Nakanishi, I., Anderson, D., 1984. Anisotropy and shear-velocity heterogeneities in the upper mantle. Geophys. Res. Lett. 11, 109–112.

Nicolas, A., Christensen, N.I., 1987. Formation of anisotropy in upper mantle peridotites: a review. In: Fuchs, K., Froidevaux, C. (Eds.), Composition, Structure and Dynamics of the Lithosphere–Asthenosphere System. In: Geodyn. Ser. AGU, Washington DC, pp. 111–123.

Panning, M., Romanowicz, B., 2006. A three-dimensional radially anisotropic model of shear velocity in the whole mantle. Geophys. J. Int. 167 (1), 361–379.

Park, J., Levin, V., 2002. Seismic anisotropy: tracing plate dynamics in the mantle. Science 296 (5567), 485–489.

Pedersen, H., Bruneton, M., Maupin, V., Tomography, S.S., 2006. Lithospheric and sublithospheric anisotropy beneath the Baltic shield from surface-wave array analysis. Earth Planet. Sci. Lett. 244 (3–4), 590–605.

Regan, J., Anderson, D., 1984. Anisotropic models of the upper mantle. Phys. Earth Planet. Inter. 35 (4), 227–263.

Ribe, N., 1989. A Continuum theory for lattice preferred orientation. Geophys. J. 97 (2), 199–207.

Ricard, Y., Bercovici, D., 2009. A continuum theory of grain size evolution and damage. J. Geophys. Res. 114, B01204. http://dx.doi.org/10.1029/2007JB005491.

Ricard, Y., Doglioni, C., Sabadini, R., 1991. Differential rotation between lithosphere and mantle – a consequence of lateral mantle viscosity variations. J. Geophys. Res. 96 (B5), 8407–8415.

Ritsema, J., Deuss, A., van Heijst, H.J., Woodhouse, J.H., 2011. S40RTS: a degree-40 shear-velocity model for the mantle from new Rayleigh wave dispersion, teleseismic traveltime and normal-mode splitting function measurements. Geophys. J. Int. 184 (3), 1223–1236.

Sharp, W.D., Clague, D.A., 2006. 50-Ma initiation of Hawaiian-Emperor bend records major change in Pacific plate motion. Science 313 (5791), 1281–1284.

Silver, P.G., Chan, W.W., 1988. Implications for continental structure and evolution from seismic anisotropy. Nature 335, 34–39.

Silver, P., Chan, W., 1991. Shear wave splitting and subcontinental mantle deformation. J. Geophys. Res. 141, 16429–16454.

Silver, P., Gao, S., Liu, K., Kaapvaal Seismic Group, 2001. Mantle deformation beneath southern Africa. Geophys. Res. Lett. 28 (13), 2493–2496.

Simons, F., van der Hilst, R., Montagner, J., Zielhuis, A., 2002. Multimode Rayleigh wave inversion for heterogeneity and azimuthal anisotropy of the Australian upper mantle. Geophys. J. Int. 151, 738–754.

Smith, D., Ritzwoller, M., Shapiro, N., 2004. Stratification of anisotropy in the Pacific upper mantle. J. Geophys. Res. 109 (B11), B11309. http://dx.doi.org/10.1029/2004JB003200.

Tanimoto, T., Anderson, D., 1984. Mapping convection in the mantle. Geophys. Res. Lett. 11 (4), 287–290.

Tommasi, A., 1998. Forward modeling of the development of seismic anisotropy in the upper mantle. Earth Planet. Sci. Lett. 160 (1–2), 1–13.

Trampert, J., Woodhouse, J., 1995. Global phase velocity maps of Love and Rayleigh waves between 40 and 150 seconds. Geophys. J. Int. 122, 675–690.

Trampert, J., Woodhouse, J., 2003. Global anisotropic phase velocity maps for fundamental mode surface waves between 40 and 150 s. Geophys. J. Int. 154, 154–165.

Turcotte, D., Schubert, G., 2002. Geodynamics, second edition. Cambridge University Press.

van Heijst, H., Woodhouse, J., 1997. Measuring surface-wave overtone phase velocities using a mode branch stripping technique. Geophys. J. Int. 131, 209–230.

Vinnik, L., Makeyeva, L., Milev, A., Usenko, A.Y., 1992. Global patterns of azimuthal anisotropy and deformations in the continental mantle. Geophys. J. Int. 111, 433–447.

Vinnik, L.P., Green, R., Nicolaysen, L., 1995. Recent deformations of the deep continental root beneath southern Africa. Nature 375, 50–52.

Wang, X., Ni, J.F., Aster, R., Sandvol, E., Wilson, D., Sine, C., Grand, S.P., Baldridge, W.S., 2008. Shear-wave splitting and mantle flow beneath the Colorado Plateau and its boundary with the Great Basin. Bull. Seismol. Soc. Am. 98 (5), 2526–2532.

Whittaker, J.M., Mueller, R.D., Leitchenkov, G., Stagg, H., Sdrolias, M., Gaina, C., Goncharov, A., 2007. Major Australian–Antarctic plate reorganization at Hawaiian-Emperor bend time. Science 318 (5847), 83–86.

Yuan, H., Romanowicz, B., 2010. Lithospheric layering in the North American craton. Nature 466 (7310), 1063–1068.

Yuan, H., Romanowicz, B., Fischer, K.M., Abt, D., 2011. 3-D shear wave radially and azimuthally anisotropic velocity model of the North American upper mantle. Geophys. J. Int. 184 (3), 1237–1260.

Zhang, S., Karato, S., 1995. Lattice preferred orientation of olivine aggregates deformed in simple shear. Nature 375 (6534), 774–777.